

Double Stage Delay Multiply and Sum Beamforming Algorithm: Application to Linear-Array Photoacoustic Imaging

Moein Mozaffarzadeh, Ali Mahloojifar*, Mahdi Orooji, Saba Adabi and Mohammadreza Nasirivanaki

Abstract—Photoacoustic imaging (PAI) is an emerging medical imaging modality capable of providing high spatial resolution of Ultrasound (US) imaging and high contrast of optical imaging. Delay-and-Sum (DAS) is the most common beamforming algorithm in PAI. However, using DAS beamformer leads to low resolution images and considerable contribution of off-axis signals. A new paradigm namely Delay-Multiply-and-Sum (DMAS), which was originally used as a reconstruction algorithm in confocal microwave imaging, was introduced to overcome the challenges in DAS. DMAS was used in PAI systems and it was shown that this algorithm results in resolution improvement and sidelobe degrading. However, DMAS is still sensitive to high levels of noise, and resolution improvement is not satisfying. Here, we propose a novel algorithm based on DAS algebra inside DMAS formula expansion, Double Stage DMAS (DS-DMAS), which improves the image resolution and levels of sidelobe, and is much less sensitive to high level of noise compared to DMAS. The performance of DS-DMAS algorithm is evaluated numerically and experimentally. The resulted images are evaluated qualitatively and quantitatively using established quality metrics including signal-to-noise ratio (*SNR*), full-width-half-maximum (*FWHM*) and contrast ratio (*CR*). It is shown that DS-DMAS outperforms DAS and DMAS at the expense of higher computational load. DS-DMAS reduces the lateral valley for about 15 dB and improves the *SNR* and *FWHM* better than 13% and 30%, respectively. Moreover, the levels of sidelobe are reduced for about 10 dB in comparison with those in DMAS.

Index Terms—Photoacoustic imaging, beamforming, linear-array imaging, noise reduction, contrast improvement.

I. INTRODUCTION

PHOTOACOUSTIC imaging (PAI) is an emerging medical imaging modality developed over the past few years and provides structural, functional and anatomical information [1], [2]. This modality uses short laser pulse to generate Ultrasound (US) waves based on thermoelastic effect and detected waves are used to reconstruct the optical absorption distribution map of the tissue [3]. The main motivation for using PAI is combining the high spatial resolution of US imaging and high contrast of optical imaging in one single imaging modality [4]. PAI is a multiscale imaging modality used in different preclinical and clinical applications e.g., tumor detection [5],

[6], ocular imaging [7], monitoring oxygenation in blood vessels [8], and functional imaging [9], [10]. There are two types of PAI: photoacoustic tomography (PAT) and photoacoustic microscopy (PAM) [11], [12]. In PAT, the induced acoustic waves are detected using an array of US transducers in the form of linear, arc or circular shape. Moreover, mathematical reconstruction algorithms are used to obtain optical absorption distribution map of the tissue [13]–[15]. There are inherent artifacts in photoacoustic (PA) reconstructed images caused by imperfect reconstruction algorithms. Reducing these artifacts has become a crucial challenge in PA image reconstruction for different number of transducers and different properties of imaging media [16]–[18].

Since PA images are obtained based on induced US signals, there are many similarities between PA and US image formation. Consequently, several US beamforming algorithms can be used in PA beamforming with some modifications [19]. These modifications have led to usage of different hardware to implement an integrated US-PA imaging device. There are many studies focused on using one beamforming technique for US and PA image formation to reduce the cost of system [20], [21]. Delay-and-Sum (DAS) can be considered as one of the most common beamforming algorithm in US imaging. However, it is a blind and non-adaptive beamformer which results in low resolution images with high levels of sidelobe [22]. The problem of a proper beamforming algorithm has been widely investigated in US imaging in different cases of study [23], [24]. The blindness of DAS algorithm can be addressed by extension of the receive aperture length in Phased Synthetic Aperture (PSA) imaging [25], and adaptive beamforming such as Minimum Variance (MV) [26]. MV adaptive beamformer, having considerable applications in RADAR and US imaging, has been modified for US imaging over the past few years in different fields of study such as complexity reduction [27], [28], US pixel-based beamforming [29], and 3D US imaging [30]. Apart from that, beamforming of plane-wave in the Fourier domain can be used to achieve fast and accurate image reconstruction [31]. Recently, Delay and Standard Deviation (DASD) beamforming algorithm was introduced in order to address the relatively poor appearance of interventional devices such as needles, guide wires, and catheters, in conventional US images [32]. To improve the quality of reconstructed images using DAS, explained in [33], Matrone et al. proposed a new beamforming algorithm namely Delay-Multiply-and-Sum (DMAS) which was used as a reconstruction algorithm in confocal microwave imaging for

*Corresponding author

M.Mozaffarzadeh, A.Mahloojifar and M.Orooji are with the Department of Biomedical Engineering, Tarbiat Modares University, Tehran, Iran (e-mail: moein.mfh@modares.ac.ir; mahlooji@modares.ac.ir; morooji@modares.ac.ir).

S.Adabi and M.Nasirivanaki are with the Department of Biomedical Engineering, Wayne State University, 818 W. Hancock, Detroit, Michigan, USA (e-mail: saba.adabi@wayne.edu; mrn.avanaki@wayne.edu).

breast cancer detection [34]. DMAS has been used with Multi-Line Transmission (MLT) for high frame-rate US imaging [35]. Both DAS and DMAS beamformers calculate delays and samples for corresponding elements of array. However, in DMAS before summation, calculated samples are combinatorially coupled and multiplied. This algorithm was recently used in PAI and it was proved that it can effectively enhance the PA images in terms of sidelobe levels and resolution [36]. In this paper, a modified version of DMAS beamformer, namely Double Stage DMAS (DS-DMAS), is introduced. By expanding the DMAS algorithm, it is proved that DMAS can be manipulated by the summation of DAS terms and it is proposed to use DMAS algorithm instead of existing DAS algorithm for all the mathematical terms.

The rest of the paper is organized as follows. Section II contains the photoacoustic wave equations and the theory of beamformers. Proposed method is introduced in section III. Numerical simulation of imaging system and experimental design along with results and performance evaluation are presented in section IV and section V, respectively. Discussion is presented in section VI and finally the conclusion is presented in section VII.

II. BACKGROUND

When PA signals are detected by linear array of US transducers, US beamforming algorithms such as DAS can be used to reconstruct the image from detected PA signals using following equation:

$$y_{DAS}(k) = \sum_{i=1}^M x_i(k - \Delta_i), \quad (1)$$

where $y_{DAS}(k)$ is the output of beamformer, k is time index, M is the number of array elements and $x_i(k)$ and Δ_i are detected signals and corresponding time delay for detector i , respectively [27]. DAS beamformer is the most common beamforming algorithm in US and PA imaging due to simple implementation and realtime imaging capability. However, this algorithm suffers from low level of off-axis signals rejection and weak suppression of interfering signals. Consequently, DAS results in reconstructed images having high levels of sidelobe and low resolution. To address incapacibilities of DAS, DMAS was suggested in [33], [36]. The same as DAS, DMAS calculates corresponding samples for each element of array based on delays, but samples are multiplied before adding them up. The DMAS formula is given by:

$$y_{DMAS}(k) = \sum_{i=1}^{M-1} \sum_{j=i+1}^M x_i(k - \Delta_i) x_j(k - \Delta_j), \quad (2)$$

To overcome the dimensionally squared problem of (2), following modifications are suggested in [33]:

$$\hat{x}_{ij}(k) = \text{sign}[x_i(k - \Delta_i) x_j(k - \Delta_j)] \sqrt{|x_i(k - \Delta_i) x_j(k - \Delta_j)|}, \quad (3)$$

for $1 \leq i \leq j \leq M$.

$$y_{DMAS}(k) = \sum_{i=1}^{M-1} \sum_{j=i+1}^M \hat{x}_{ij}(k). \quad (4)$$

Performing sign, absolute and square root after coupling procedure in (3) and (4), which requires $(M^2 - M)/2$ computations for each pixel, result in slow imaging. To put it more simply, sometimes these library functions require many clock cycles which leads to improper timing performance of DMAS algorithm. Applying following procedure to the received PA signals reduces computational number of the sign, absolute and square root operations to M for each pixel [36]:

$$\bar{x}_i(k) = \text{sign}[x_i(k)] \sqrt{x_i(k)}, \quad \text{for } 1 \leq i \leq M. \quad (5)$$

$$\hat{x}_{ij}(k) = \bar{x}_i(k) \bar{x}_j(k), \quad \text{for } 1 \leq i \leq j \leq M. \quad (6)$$

The procedure of DMAS algorithm can be considered as a correlation process which uses the autocorrelation of the aperture. In other words, the output of this beamformer is the spatial coherence of detected PA signals and it is a non-linear beamforming algorithm.

III. PROPOSED METHOD

In this paper, DMAS beamforming is proposed to be used instead of the existing DAS algorithm inside DMAS algebra. Initially, consider the expansion of DMAS algorithm, which can be written as follows:

$$\begin{aligned} y_{DMAS}(k) &= \sum_{i=1}^{M-1} \sum_{j=i+1}^M x_{id}(k) x_{jd}(k) = \\ & x_{1d}(k) [x_{2d}(k) + x_{3d}(k) + x_{4d}(k) + \dots + x_{Md}(k)] \\ & + x_{2d}(k) [x_{3d}(k) + x_{4d}(k) + \dots + x_{Md}(k)] \\ & + \dots \\ & + x_{(M-2)d}(k) [x_{(M-1)d}(k) + x_{Md}(k)] \\ & + [x_{(M-1)d}(k) x_{Md}(k)], \end{aligned} \quad (7)$$

where $x_{id}(k)$ and $x_{jd}(k)$ are delayed detected signals for element i and j , respectively. According to (7), there is a DAS in each term of the expansion, which can be used to generate DS-DMAS beamformer as follows:

$$\begin{aligned} y_{DMAS}(k) &= \sum_{i=1}^{M-1} \sum_{j=i+1}^M x_{id}(k) x_{jd}(k) = \\ & \underbrace{[x_{1d}(k) x_{2d}(k) + x_{1d}(k) x_{3d}(k) + \dots + x_{1d}(k) x_{Md}(k)]}_{\text{first term}} \\ & + \underbrace{[x_{2d}(k) x_{3d}(k) + x_{2d}(k) x_{4d}(k) + \dots + x_{2d}(k) x_{Md}(k)]}_{\text{second term}} \\ & + \dots \\ & + \underbrace{[x_{(M-2)d}(k) x_{(M-1)d}(k) + x_{(M-2)d}(k) x_{Md}(k)]}_{\text{(M-2)th term}} \\ & + \underbrace{[x_{(M-1)d}(k) x_{Md}(k)]}_{\text{(M-1)th term}}. \end{aligned} \quad (8)$$

DMAS algorithm is a correlation process in which for each point of the image, calculated delays for each element of the

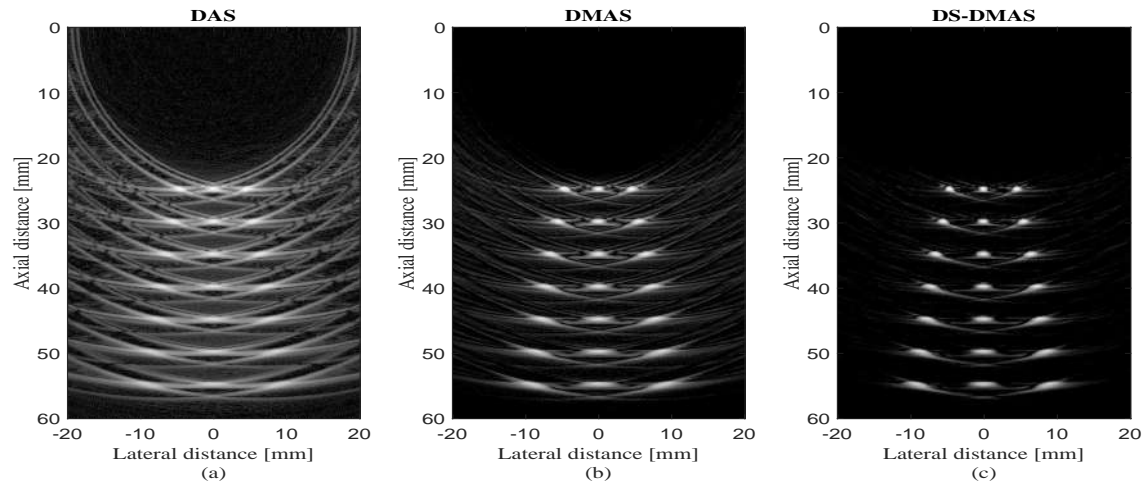


Fig. 1: Simulated three-point target using linear array. (a) DAS, (b) DMAS and (c) DS-DMAS. All images are shown with a dynamic range of 60 dB. 50 dB noise was added to detected signals.

array are combinatorially coupled and multiplied and the similarity of samples are obtained. In (8), there is a summation as a type of DAS algebra between all the terms. If the contribution of off-axis signals result in a high error in correlation process of DMAS, then summation of calculated correlations leads to summation of high range of error. It is proposed to use DMAS beamformer between each term of expansion instead of DAS, in which the samples go through another correlation procedure. To illustrate, consider the following equation:

$$y_{DS-DMAS}(k) = \sum_{i=1}^{M-2} \sum_{j=i+1}^{M-1} x_{it}(k)x_{jt}(k), \quad (9)$$

where x_{it} and x_{jt} are the i_{th} and j_{th} term shown in (8). The expansion of DS-DMAS beamformer can be written as:

$$\begin{aligned} y_{DS-DMAS}(k) &= \sum_{i=1}^{M-2} \sum_{j=i+1}^{M-1} x_{it}(k)x_{jt}(k) = \\ &x_{1t}(k) \left[x_{2t}(k) + x_{3t}(k) + x_{4t}(k) + \dots + x_{(M-1)t}(k) \right] \\ &+ x_{2t}(k) \left[x_{3t}(k) + x_{4t}(k) + \dots + x_{(M-1)t}(k) \right] \\ &+ \dots \\ &+ x_{(M-3)t}(k) \left[x_{(M-2)t}(k) + x_{(M-1)t}(k) \right] \\ &+ \left[x_{(M-2)t}(k)x_{(M-1)t}(k) \right]. \end{aligned} \quad (10)$$

Since DAS is a non-adaptive beamformer and considers all calculated samples for each element of array identically, the acquired image by every term can blur the final reconstructed image. Using (10), blurring can be prevented and the noise of the reconstructed images can be reduced. Of note, the same procedure that was introduced in (5) and (6) in order to speed up the DMAS beamformer, is used in DS-DMAS for the same reason. In the section IV it is shown that DS-DMAS beamformer results in resolution improvement, and significant high level of noise and sidelobe reduction.

IV. NUMERICAL RESULTS AND PERFORMANCE ASSESSMENT

In this section, numerical results are presented to illustrate the performance of the proposed algorithm in comparison with DMAS and DAS.

A. Simulated Point Target

K-wave Matlab toolbox was used to simulate the numerical study [37]. Twenty-one 0.1 mm spherical absorbers were positioned along the vertical axis every 5 mm as initial pressure. The first absorber was 25 mm away from the transducer surface. Each two absorbers at each depth were away 4.6 mm, 5.5 mm, 6.4 mm, 7.2 mm, 7.7 mm, 8.5 mm and 9.1 mm laterally from each other. Imaging region was 40 mm in lateral axis and 60 mm in vertical axis. Linear array having $M=128$ elements operating at 7 MHz central frequency and 77 % fractional bandwidth was used to detect the PA signals generated from defined initial pressures. Speed of sound was assumed to be 1540 m/s during simulations. 50 dB and 10 dB Gaussian noise was added to detected signals. Envelope detection, performed by means of the Hilbert transform, has been used in the end for all presented images, and the obtained lines are normalized and log-compressed to form the final images.

In Fig. 1, results of beamforming algorithms are shown, where 50 dB noise is added to the detected signals. Fig. 1(a), Fig. 1(b) and Fig. 1(c) show the output of DAS, DMAS and DS-DMAS beamformer, respectively. The comparison of DMAS and DAS reveals that DMAS beamformer results in more distinguishable point targets in all depths of imaging, while DAS beamformer results in high levels of sidelobe and a low resolution image. In addition, point targets are hardly distinguishable after imaging depth of 35 mm using DAS beamformer. By comparing reconstructed images using DS-DMAS and DMAS beamformers, it can be perceived that DS-DMAS leads to lower levels of sidelobe and more distinguished point targets. To compare the different beamforming

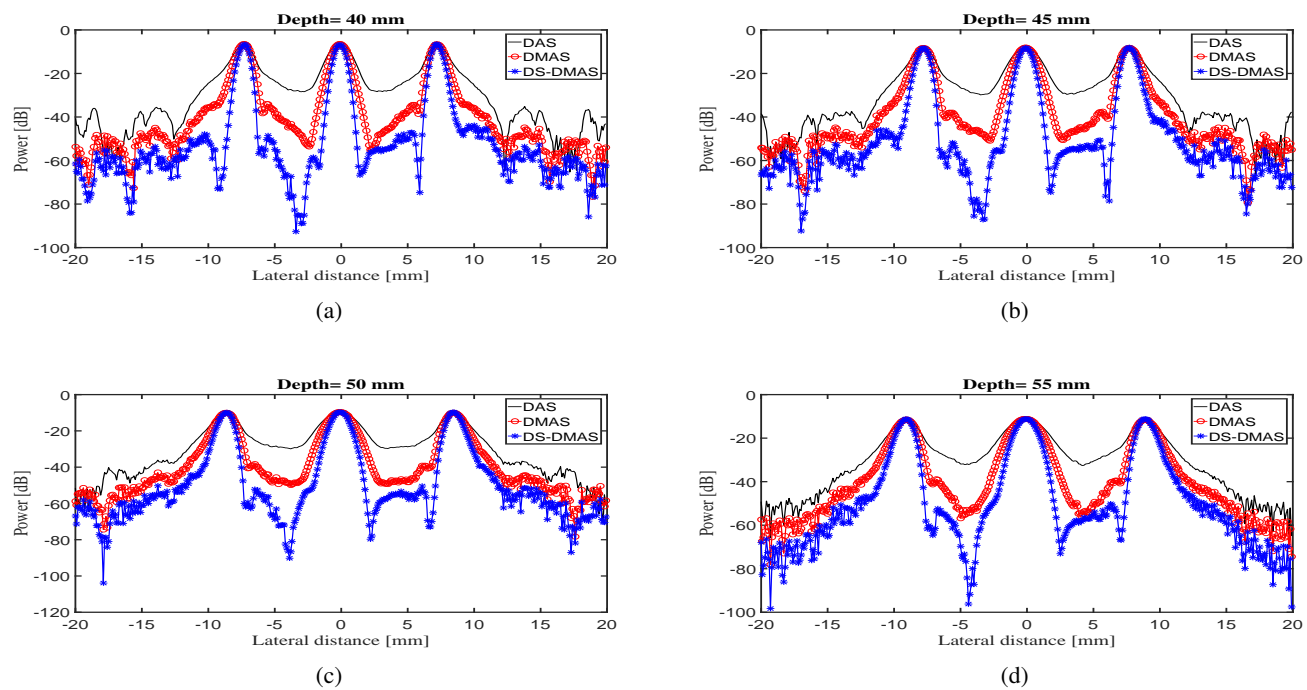


Fig. 2: Lateral variation of DAS, DMAS, DS-DMAS in depth of (a) 40 mm, (b) 45 mm, (c) 50 mm and (d) 55 mm.

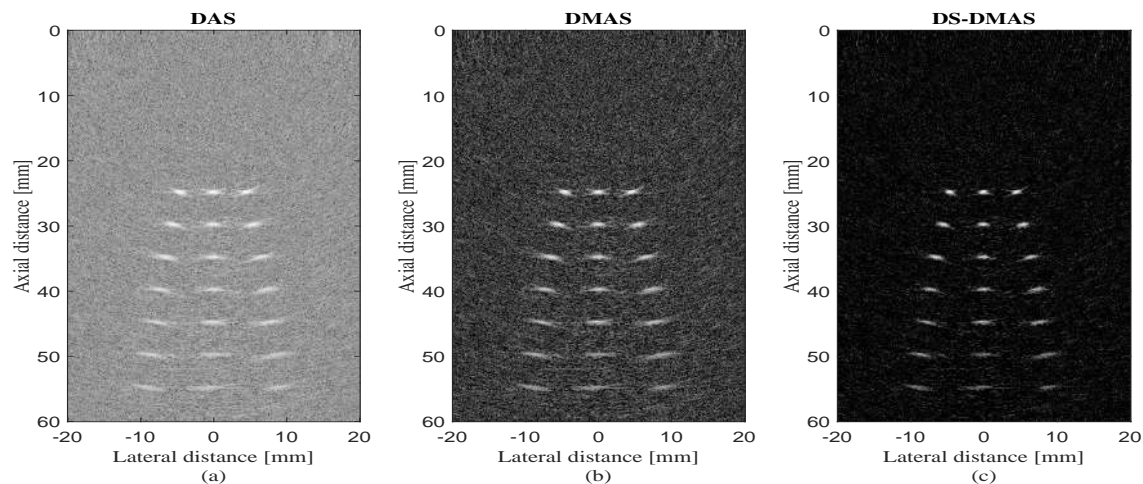


Fig. 3: Simulated three-point target using linear array. (a) DAS, (b) DMAS and (c) DS-DMAS. All images are shown with a dynamic range of 60 dB. 10 dB noise was added to detected signals.

algorithms in detail, the lateral variations of images formed by mentioned beamformers are presented in Fig. 2, where 50 dB noise is added to the detected signals. Lateral variations in depth of 40 mm, 45 mm, 50 mm and 55 mm are shown in Fig. 2(a), Fig. 2(b), Fig. 2(c) and Fig. 2(d), respectively. It can be seen that sidelobe levels using DS-DMAS has the lowest level in comparison with two other algorithms in all depths of imaging, for instance, consider the depth of 55 mm where sidelobe levels of DAS, DMAS and DS-DMAS are about -42 dB, -58 dB and -72 dB, respectively. This conclusion can be perceived considering all the lateral variations in all depths of imaging. According to Fig. 2, DS-DMAS beamformer leads to higher resolution in comparison with DAS and DMAS. In other words, by comparing the valley of lateral variations for

mentioned beamformers, resolution elevation can be achieved. In particular, at depth of 50 mm, valley of lateral variation is reduced for about 30 dB, 51 dB and 63 dB for DAS, DMAS and DS-DMAS, respectively. Consequently, DS-DMAS results in more distinguished point targets and higher resolution in comparison to other beamformers. To conclude, in all depths of imaging DS-DMAS outperforms DAS and DMAS in cases of resolution and sidelobe levels. The three-point target simulation has been implemented in the presence of a high level of noise to evaluate the performance of beamformers in case of noise reduction. The reconstructed PA images are shown in Fig. 3, where 10 dB Gaussian noise was added to the detected signals. Also, lateral variation of reconstructed images using noisy signals is shown in Fig. 4.

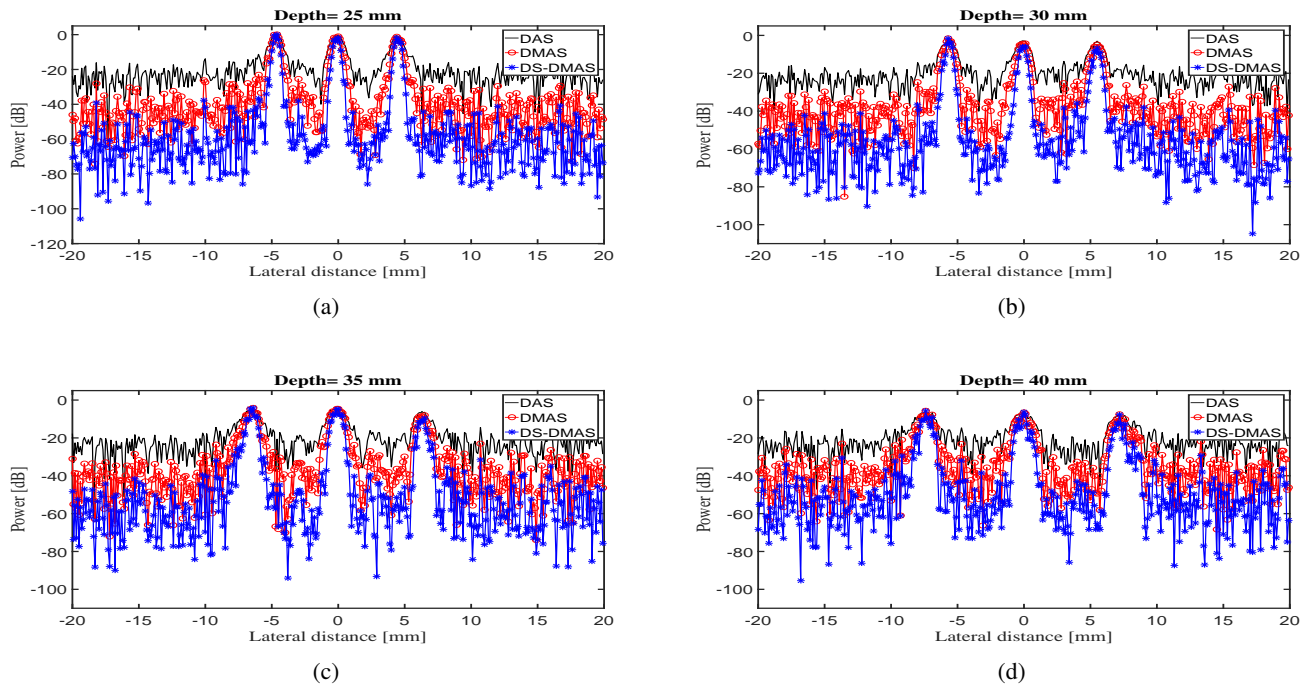


Fig. 4: Lateral variation of DAS, DMAS and DS-DMAS in depth of (a) 25 mm, (b) 30 mm, (c) 35 mm and (d) 40 mm.

TABLE I: SNR (dB) Values in Different Depths.

Depth(mm)	50dB noise		
	DAS	DMAS	DS-DMAS
25	34.8216	47.4809	53.6078
30	33.8332	44.9784	50.3456
35	33.0357	43.7758	48.8758
40	32.2885	42.0026	47.3446
45	31.1803	40.2071	45.335
50	30.1526	38.5532	43.7768
55	29.314	37.3118	42.9101

TABLE II: FWHM (mm) Values in Different Depths.

Depth(mm)	50dB noise		
	DAS	DMAS	DS-DMAS
25	0.8613	0.5825	0.3931
30	1.0337	0.6299	0.463
35	1.165	0.8034	0.5288
40	1.3973	0.9735	0.6603
45	1.666	1.1767	0.8
50	1.985	1.4096	1.0356
55	2.2668	1.6922	1.2376

As can be seen in Fig. 3, the presence of noise is obvious in the reconstructed image using DAS beamformer and after depth of 45 mm the point-targets are barely detectable. DMAS beamformer leads to more noise reduction and reconstructed image contains a lower levels of noise in comparison with DAS, but effect of noise still suffers the reconstructed image. As shown Fig. 3, DS-DMAS results in more noise reduction and reconstructed image has a higher quality in comparison with DAS and DMAS. To compare the sidelobe levels and noise reduction of proposed algorithm and two other beamformers, lateral variations in four depths of imaging are presented in Fig. 4. Lateral variation in depth of 25 mm, 30 mm, 35 mm and 40 mm are shown in Fig. 4(a), Fig. 4(b), Fig. 4(c) and Fig. 4(d), respectively. Clearly, sidelobe levels of DS-DMAS beamformer has the lowest level in comparison with DAS and DMAS, for instance, at the depth of 40 mm, sidelobe levels for DAS, DMAS and DS-DMAS are for about -20 dB, -40 dB and -60 dB, respectively. Consequently, DS-DMAS results in 40 dB and 20 dB sidelobe levels reduction in comparison to DAS and DMAS, respectively.

To quantitatively compare the performance of the beamformers, signal-to-noise ratio (SNR) and full-width-half-maximum (FWHM) in -3 dB are calculated in all depths

of imaging using points positioned axially in all depths and 0 mm lateral distance, shown in Fig. 1. The results are shown in Table I and Table II for SNR and FWHM, respectively. SNR is calculated using following equation:

$$SNR = 20 \log_{10} P_{signal} / P_{noise}. \quad (11)$$

where P_{signal} and P_{noise} are difference of maximum and minimum intensity of each region, and standard deviation of the region, respectively. Considering Table I, in all depths of imaging DMAS and DS-DMAS beamformers outperform DAS. In particular, the depth of 50 mm where SNR of DAS, DMAS and DS-DMAS is for about 30.1526 dB, 38.5532 dB and 43.7768 dB, respectively. In other words, DS-DMAS results in higher SNR for about 13.6242 dB and 5.2236 dB in compare to DMAS and DAS, respectively. The outperforming of DS-DMAS beamformer in all depths of imaging is clear by considering presented results in the Table I. To evaluate the performance of proposed method in case of FWHM, consider Table II where results show that mentioned DMAS based algorithms outperform DAS, while DS-DMAS leads to narrower mainlobe width in all depths of imaging in compare to DMAS. For instance, consider depth of 55 mm where DAS, DMAS and DS-DMAS leads to 2.2668 mm 1.6922

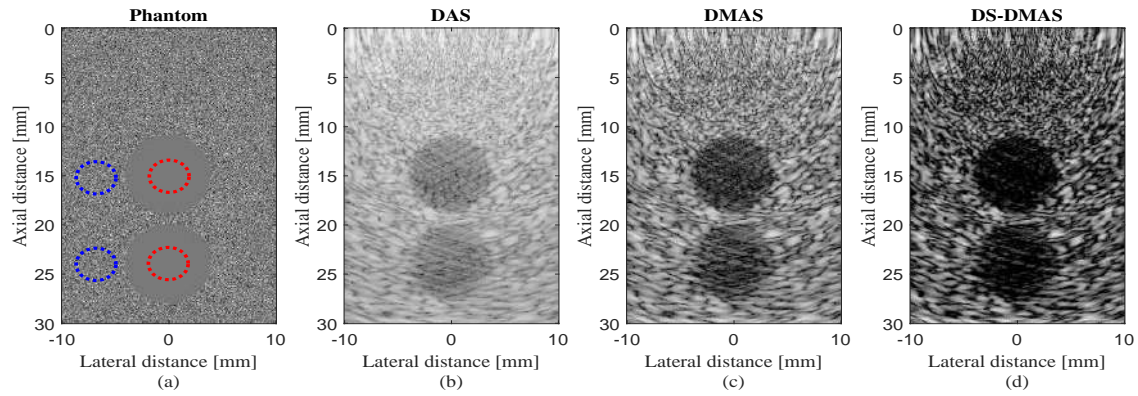


Fig. 5: Simulated cyst target using linear array. (a) Phantom, (b) DAS, (c) DMAS and (d) DS-DMAS. All images are shown with a dynamic range of 60 dB. 50 dB noise was added to detected signals.

mm 1.2376 mm. It implies that resolution is improved using DS-DMAS in compare to DMAS and DAS. Moreover, the variation of $FWHM$, as long as depth of imaging increases, becomes less using DS-DMAS. In other words, differentiation of $FWHM$ in the first depth and the last depth of imaging results in 1.4055 mm, 1.1094 mm and 0.8445 mm for DAS, DMAS and DS-DMAS, respectively. Therefore, as long as depth of imaging increases, resolution degrades more slowly using DS-DMAS in compare to DMAS and DAS.

B. Simulated Circular Cyst

Two cysts having radius of 4 mm are located at depth of 15 mm and 24 mm. Phantom of imaging, and reconstructed images using DAS, DMAS and DS-DMAS are shown in Fig. 5(a), Fig. 5(b), Fig. 5(c) and Fig. 5(d), respectively. The contrast ratio (CR) metric was used to quantitatively evaluate the performance of beamformers under cyst targets. CR index is defined as:

$$CR = 20 \log_{10} \left(\frac{\mu_{cyst}}{\mu_{bck}} \right) \quad (12)$$

where μ_{cyst} and μ_{bck} are the mean of image intensity before log compression inside the red and blue dotted circle in Fig. 5(a), respectively. Table III represents the calculated CR using each beamformer for two cysts located at two depths. As can be seen in depth of 15 mm, DMAS and DS-DMAS beamformers lead to 12.5727 dB and 21.591 dB CR enhancement in compare to DAS, respectively. Moreover, DS-DMAS causes 9.0183 dB CR enhancement in compare to DMAS. In the other hand, for cyst located at depth of 24 mm DMAS-based algorithms outperform DAS beamformer while DS-DMAS results in 7.388 dB improvement in CR parameter in compare to DMAS beamformer.

TABLE III: Contrast Ratio (dB) Parameter For the Two Cysts Phantom.

Beamformer	15 mm	24 mm
DAS	-14.9420	-10.9521
DMAS	-27.5147	-20.0327
DS-DMAS	-36.5330	-27.4207

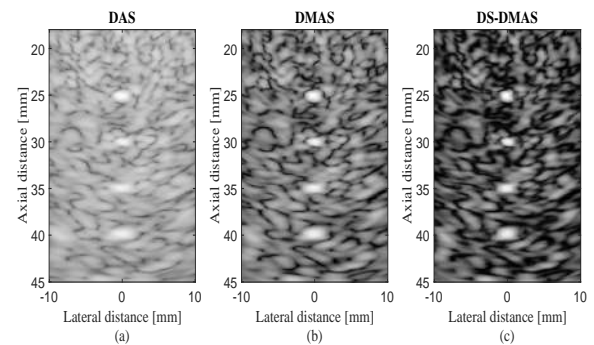


Fig. 6: Simulated point targets positioned in a low contrast background using linear array. (a) DAS, (b) DMAS and (c) DS-DMAS. All images are shown with a dynamic range of 60 dB. 50 dB noise was added to detected signals.

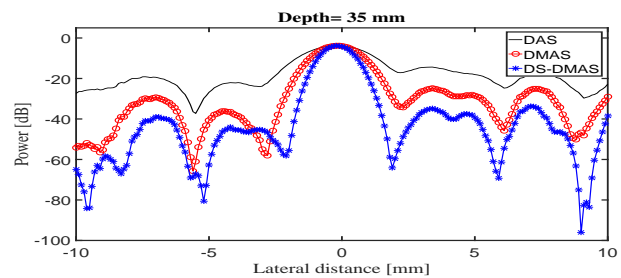


Fig. 7: Lateral variation of DAS, DMAS and DS-DMAS in depth of 35 mm.

C. Low Contrast Target

In this section, DS-DMAS beamformer is evaluated using low contrast targets. Four 0.1 mm spherical absorbers were positioned along the vertical axis every 5 mm as initial pressure. The first absorber was 25 mm away from the transducer surface. Imaging region was 20 mm in lateral axis and 45 mm in vertical axis. As can be seen in Fig. 6, point targets are more detectable in formed image using DS-DMAS while the background of imaging medium is retained. In order to compare beamformers in detail, lateral variation for each beamformer at the depth of 35 mm is presented in Fig. 7. As is shown, DS-DMAS results in a narrower mainlobe. Moreover,

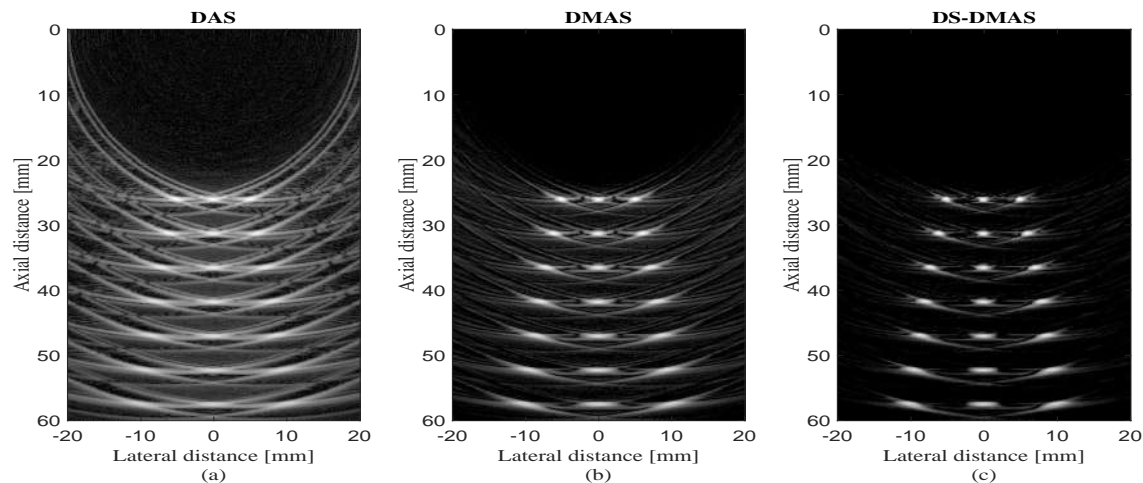


Fig. 8: Simulated three-point target using linear array. (a) DAS, (b) DMAS and (c) DS-DMAS. All images are shown with a dynamic range of 60 dB. 50 dB noise was added to detected signals. The sound velocity is overestimated about 5%.

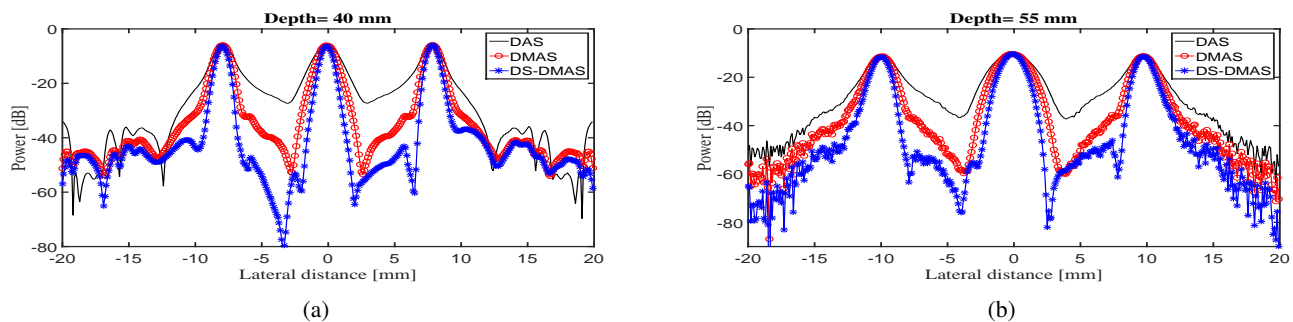


Fig. 9: Lateral variation of DAS, DMAS and DS-DMAS in depth of (a) 40 mm, (b) 55 mm. The sound velocity is overestimated about 5%.

DS-DMAS reduces the sidelobe levels for about 23 dB and 11 dB in comparison with DAS and DMAS, respectively.

D. Sensitivity to Sound Velocity Inhomogeneities

In this section, the proposed method is evaluated in the term of robustness against the sound velocity errors resulting from medium inhomogeneities that are inevitable in practical imaging. The simulation design for Fig. 1 is used in order to investigate the robustness, except that the sound velocity is overestimated by 5%, which covers and may be more than the typical estimation error [38]. As can be seen in Fig. 8(a), the reconstructed image using DAS is suffering from negative effects of overestimated sound velocity. DMAS reduces the negative effects, and reconstructed image using DMAS, shown in Fig. 8(b), contains lower levels of artifacts. Even though the peak amplitudes are well estimated by DMAS, the negative effects are still annoying. As can be seen in Fig. 8(c), DS-DMAS reduces the effects of overestimated sound velocity in the reconstructed image and provides a higher image quality in comparison with DAS and DMAS. More importantly, the peak amplitudes are estimated the same as DAS and DMAS. Fig. 9 shows the lateral variation of the reconstructed images

in Fig. 8. As can be seen, in the both presented depths, DS-DMAS results in the narrower mainlobe and lower levels of sidelobe in comparison with DAS and DMAS.

E. Processing Complexity

In order to compare proposed method with other beamformers in term of computational burden, the number of operations needed for each algorithm are presented in Table IV. As can be seen, the order of computational complexity for DS-DMAS and DMAS is $O(M^2)$ which is exponentially more than $O(M)$ for DAS. This is the cost that is paid for higher performance of DMAS and DS-DMAS in comparison with DAS. On the other hand, the overhead computational cost of DS-DMAS in compare to DMAS, is linearly increased by increasing the number of employed elements of the transducer.

TABLE IV: Processing Complexity for Different Beamformers.

Beamformer	Number of Operations
DAS	M
DMAS	$\frac{M(M-1)}{2} + 2(M-1)$
DS-DMAS	$M(M-1) + 3(M-1)$

V. EXPERIMENTAL RESULTS

To evaluate the DS-DMAS beamformer, in this section results of designed experiments are presented. A linear-array of PAI system was used to detect the PA waves and the major components of the system include an US data acquisition system, vantage 128 Verasonics (Verasonics, Inc., Redmond, WA), a Q-switched Nd:YAG laser with a pulse repetition rate of 25 Hz, wavelength 532 nm and a pulse width of 10 ns. A transducer array (L7-4, Philips Healthcare) having 128 elements and 5.2080 MHz central frequency was used as a receiver. A function generator is used to synchronize all operations (i.e., laser firings, PA signal recording). The sampling frequency on the receive is for about 20.8320 MHz and the schematic of designed imaging system is presented in Fig. 10. Eight wires as absorbers were positioned along vertical axis, beginning 20 mm from transducer surface, while each two wires at each depth are almost parallel. The system positioning is shown in Fig. 11 and it should be noticed that transducer surface is perpendicular to wires, so it is expected to provide a cross-section of the wires. The reconstructed images are shown in Fig. 12. As can be seen, DAS results in a low quality image with high level of artifacts, while DMAS enhances the reconstructed images. Although using DMAS results in an image with higher quality, it still suffers from artifacts. DS-DMAS leads to more enhanced image in compare to DAS and DMAS and also more noise reduction and levels of sidelobe degrading. To illustrate, consider the lateral variation of reconstructed images shown in Fig. 13, where lateral variations for two depths of imaging are presented. As can be seen in Fig. 13(a), sidelobe level using DAS is for about -30 dB, while using DMAS results in about 20 dB sidelobe level reduction in compare to DAS and finally DS-DMAS leads to -65 dB sidelobe level, which is the lowest sidelobe

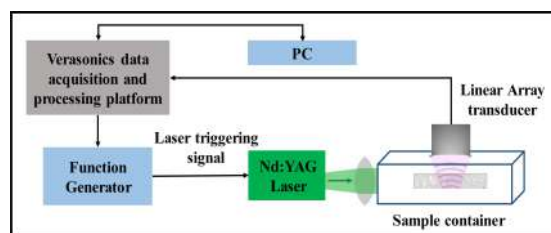


Fig. 10: Schematic of experimental setup.

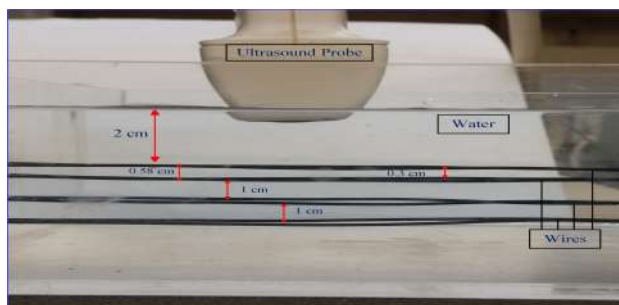


Fig. 11: Experimental setup of PA linear array imaging of eight wires.

level among mentioned beamformers. Moreover, the valley of lateral variation in both presented depths of imaging has the lowest level using DS-DMAS. Consider, in particular, depth of 20 mm shown in Fig. 13(a), where DAS, DMAS and DS-DMAS result in -40 dB, -52 dB and -63 dB valley of lateral variation, respectively. As a result, in both presented lateral variation, DS-DMAS results in the lowest level of sidelobes and artifacts, while point-targets are still detectable. Table V represents the calculated SNR in two depths of imaging, shown by the yellow circles in Fig. 12. As can be perceived, DS-DMAS results in higher SNR in comparison with DAS and DMAS. In particular, consider the depth of 20 mm where DS-DMAS leads to SNR improvement for about 23.1804 dB and 11.9131 dB in comparison to DAS and DMAS, respectively. In order to investigate the resolution in higher precision, another experiment has been developed. In Fig. 14, reconstructed images using two wires as targets are shown. As can be seen in Fig. 15(a) and Fig. 15(b), DS-DMAS results in a narrower mainlobe and lower levels of sidelobe in comparison with DAS and DMAS. FWHM metric is presented in Table VI for two detected targets in Fig. 14. Consider, in particular, the depth of 30 mm where DS-DMAS results in FWHM improvement for about 0.9257 mm and 0.4252 mm in comparison with DAS and DMAS, respectively.

VI. DISCUSSION

The main enhancements gained by proposed beamforming algorithm are high noise reduction and artifact suppression. As can be seen in Fig. 1(a), Fig. 3(a), Fig. 8(a), Fig. 12(a) and Fig. 14(a), reconstructed images using DAS leads to high levels of sidelobe and artifacts which result from its inherent non-adaptiveness, blindness and high contribution of off-axis signals. Due to the combinatory coupling, multiplication and sum of the detected PA waves, reconstructed images using DMAS are improved in the cases of contrast resolution and contribution of noise. In other words, since DMAS algorithm calculates the auto-correlation of received PA signals, the output of this beamformer is the coherence of detected PA signals, and each calculated sample is weighted based on other calculated samples. This procedure of weighting makes DMAS away from blindness exists in DAS. It can be seen in Fig. 1(b), Fig. 3(b), Fig. 8(b), Fig. 12(b) and Fig. 14(b) that DMAS results in the higher quality images and more noise reduction. The contribution of off-axis signals leads to

TABLE V: SNR (dB) Values in Two Depths of Imaging.

Beamformer	20 mm	28 mm
DAS	32.9036	26.735
DMAS	44.1709	34.2061
DS-DMAS	56.0840	43.7240

TABLE VI: FWHM (mm) Values in Two Depths of Imaging.

Beamformer	30 mm	50 mm
DAS	1.4059	0.7384
DMAS	0.9054	0.4789
DS-DMAS	0.4802	0.3756

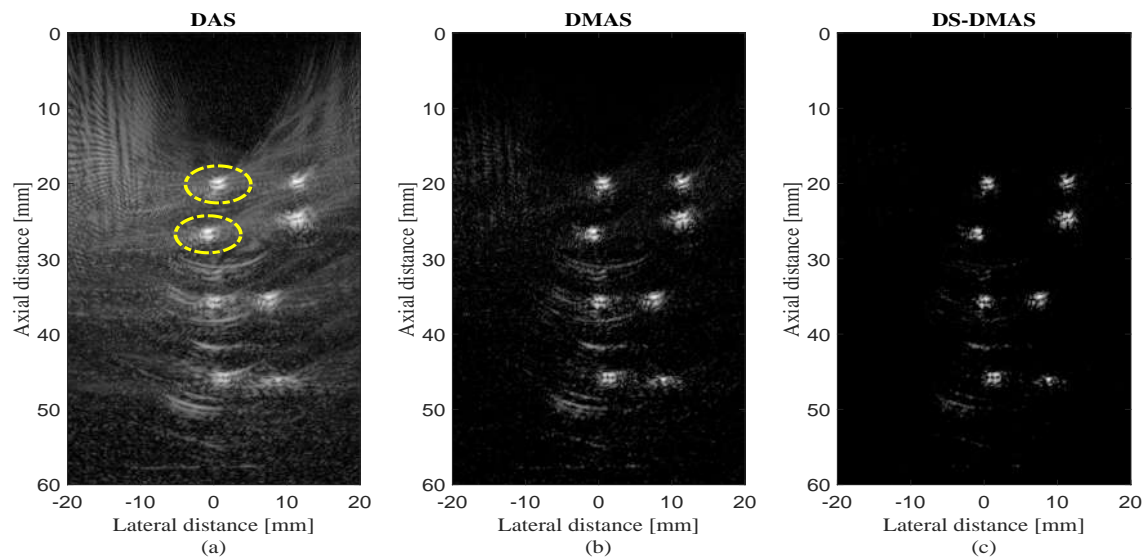


Fig. 12: Reconstructed experimental images using linear array. (a) DAS, (b) DMAS and (c) DS-DMAS. All images are shown with a dynamic range of 50 dB.

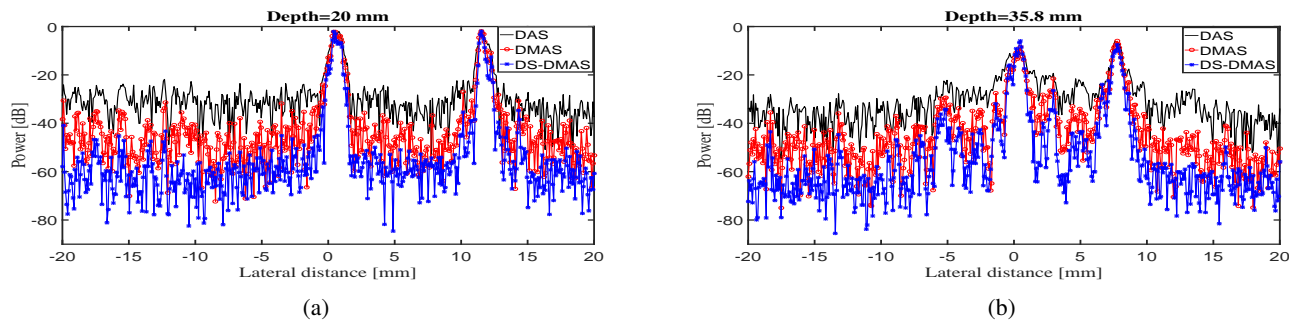


Fig. 13: Lateral variation of DAS, DMAS and DS-DMAS in depth of (a) 20 mm and (b) 35.8 mm.

high levels of artifacts in the output of DAS beamformer while many of these suffering effects are addressed using DMAS and its correlation procedure. However, if the levels of artifacts increase, which mostly happens in high depths of imaging, or if imaging medium includes high levels of noise, the correlation procedure of DMAS will not be able to address the annoying effects. The effects of contribution of off-axis signals and high level of noise using DMAS can be seen in Fig. 1(b), Fig. 3(b) and Fig. 8(b), where quality of reconstructed point-target gets worse as depth of imaging increases. Also, it can be seen in Fig. 2 that although DMAS results in lower levels of sidelobe and a narrower width of mainlobe in compare to DAS, as depth of imaging increases the resolution and quality of reconstructed point-target get worse.

Expansion of DMAS beamformer algorithm is presented in (7) and (8), where there is a DAS between each term of the expansion. Consequently, if effect of off-axis signals and noise are presented, the quality of the reconstructed image will not be as expected. Since DMAS has been proved to be helpful in noise reduction and contrast resolution enhancement, this

beamformer can be used instead of existing DAS inside DMAS algorithm expansion. To put it more simply, it is proposed to address the effects of high level of medium noise and contribution of off-axis signals using another correlation process inside DMAS. In DMAS, each calculated sample for each element is weighted based on detected signals using other elements of the array. The high level of medium noise and contribution of off-axis signals can prevent DMAS in (7) to weight samples correctly. DS-DMAS modifies the calculated weights using two stages of DMAS. As can be seen in Fig. 1(c) and Fig. 2, sidelobe levels and negative effect of DMAS are degraded using DS-DMAS and reconstructed point target are more detectable, especially in high depths of imaging. Considering Fig. 3(c) and Fig. 4, it can be perceived that DS-DMAS results in more enhanced image in the presence of high level of medium noise in comparison to DMAS and DAS. All simulations and calculated parameters indicate that DS-DMAS beamformer outperforms DMAS and DAS in all parameters at the expense of more number of operations in compare to DMAS and DAS. Of note, it is expected that DS-DMAS uses the strong signals and discards the weak signals.

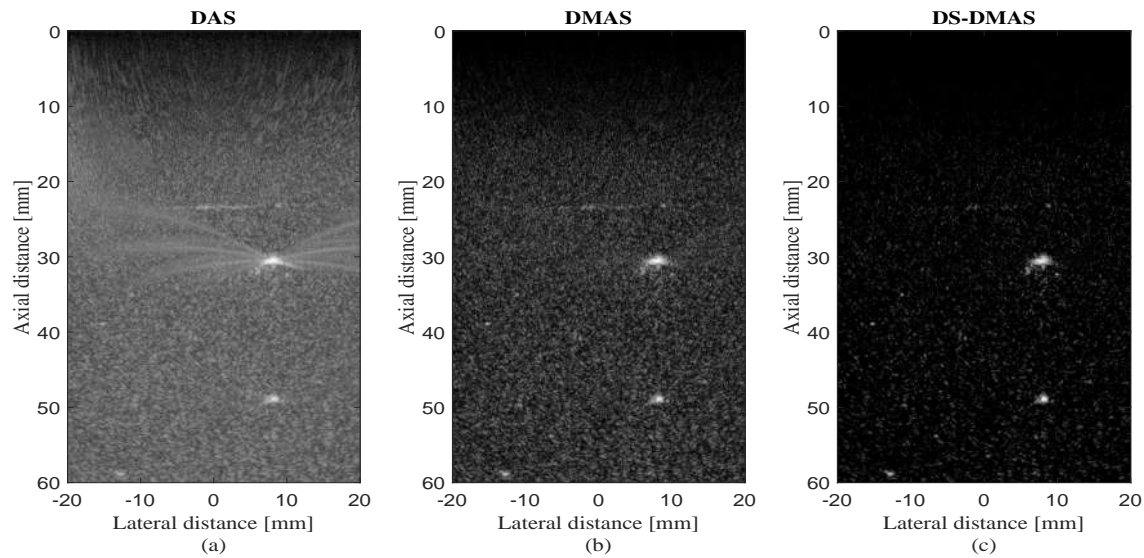


Fig. 14: Reconstructed experimental images using linear array. (a) DAS, (b) DMAS and (c) DS-DMAS. All images are shown with a dynamic range of 60 dB.

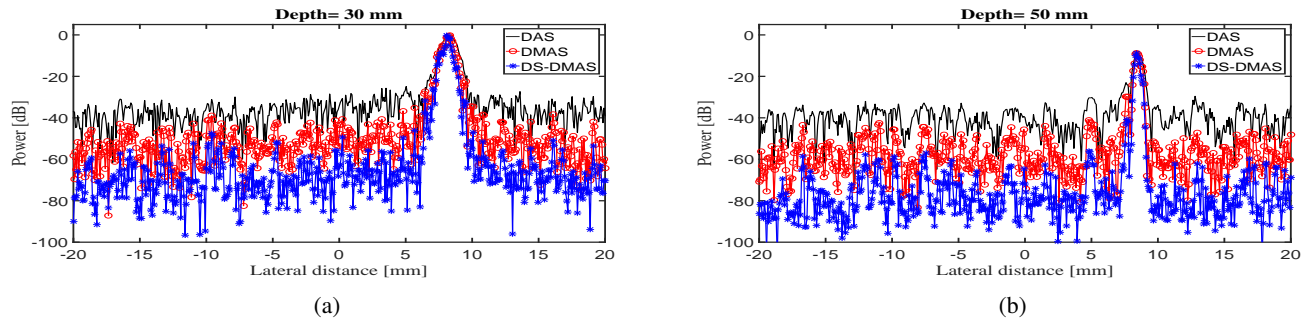


Fig. 15: Lateral variation of DAS, DMAS and DS-DMAS in depth of (a) 30 mm and (b) 50 mm.

In Fig. 6, performance of DS-DMAS has been evaluated using point targets having low contrast in comparison with the imaging medium. Based on visual evaluation and presented lateral variation in Fig. 7, DS-DMAS provides images with higher quality in comparison to DAS and DMAS in case of low contrast targets. In order to investigate the robustness of proposed method, sound velocity has been overestimated in reconstruction procedure. Formed images are shown in Fig. 8, and corresponding lateral variations in two depths of imaging are presented in Fig. 9. DS-DMAS estimates the peaks amplitude correctly while reduces the negative effects of overestimated sound velocity. Reconstructed images using experimental data are shown in Fig. 12 and Fig. 14. As can be seen, reconstructed images using DS-DMAS contains lower levels of sidelobe and artifacts. In other words, DS-DMAS retains strong signals while degrading the weak signals in order to form images with higher quality in compare to DMAS and DAS. Lateral variations of experimental reconstructed images are presented in Fig. 13 and Fig. 15, which show DS-DMAS outperforms DAS and DMAS in the terms of levels of sidelobe. Moreover, the *SNR* metric for experimental

images, shown in Fig. 13, are presented in Table V and show the superiority of DS-DMAS in comparison with DAS and DMAS. Apart from that, resolution improvement can be seen in Fig. 15, along with corresponding *FWHM* metric presented in Table VI.

VII. CONCLUSION

In PAI, DAS beamformer the most common image reconstruction algorithm due to its simple implementation, formed image suffers from poor resolution and high levels of sidelobe. To overcome these limitations, DMAS algorithm was proposed, which was recently used in US imaging. DMAS beamformer is based on the correlation of detected signals at the elements of the array and expanding DMAS formula leads to multiple terms of DAS. In this paper, we introduced a modified version of DMAS beamforming algorithm, called DS-DMAS. This algorithm is based on existing DAS in the expansion of DMAS algorithm and it is proposed to use DMAS instead of existing DAS in the expansion. It has been shown that using DMAS-based algorithms leads to sidelobes levels reduction and resolution improvement in comparison

with DAS, while DS-DMAS outperforms DMAS. Numerical simulations using three-point target at different depths of imaging and two levels of noise, along with cyst target and experimental results are presented. Results are discussed for each beamforming algorithm in terms of sidelobe levels, resolution. The qualitative and quantitative comparisons show that DS-DMAS beamformer significantly reduces levels of sidelobe for about 15 dB and improves resolution. Moreover, DS-DMAS leads to improvement in terms of SNR, FWHM and CR for about 13% , 30% and 35% in compare to DMAS, respectively.

REFERENCES

- [1] J. Xia and L. V. Wang, "Small-animal whole-body photoacoustic tomography: a review," *IEEE Transactions on Biomedical Engineering*, vol. 61, no. 5, pp. 1380–1389, 2014.
- [2] M. Xu and L. V. Wang, "Photoacoustic imaging in biomedicine," *Review of Scientific Instruments*, vol. 77, no. 4, p. 041101, 2006.
- [3] M. Jeon and C. Kim, "Multimodal photoacoustic tomography," *IEEE Transactions on Multimedia*, vol. 15, no. 5, pp. 975–982, 2013.
- [4] J. Kim, D. Lee, U. Jung, and C. Kim, "Photoacoustic imaging platforms for multimodal imaging," *Ultrasonography*, vol. 34, no. 2, p. 88, 2015.
- [5] B. Guo, J. Li, H. Zmuda, and M. Sheplak, "Multifrequency microwave-induced thermal acoustic imaging for breast cancer detection," *IEEE Transactions on Biomedical Engineering*, vol. 54, no. 11, pp. 2000–2010, 2007.
- [6] M. Heijblom, W. Steenbergen, and S. Manohar, "Clinical photoacoustic breast imaging: the twente experience," *IEEE Pulse*, vol. 6, no. 3, pp. 42–46, 2015.
- [7] A. de La Zerda, Y. M. Paulus, R. Teed, S. Bodapati, Y. Dollberg, B. T. Khuri-Yakub, M. S. Blumenkranz, D. M. Moshfeghi, and S. S. Gambhir, "Photoacoustic ocular imaging," *Optics letters*, vol. 35, no. 3, pp. 270–272, 2010.
- [8] R. O. Esenaliev, I. V. Larina, K. V. Larin, D. J. Deyo, M. Motamedi, and D. S. Prough, "Optoacoustic technique for noninvasive monitoring of blood oxygenation: a feasibility study," *Applied Optics*, vol. 41, no. 22, pp. 4722–4731, 2002.
- [9] J. Yao, J. Xia, K. I. Maslov, M. Nasirivanaki, V. Tsytarev, A. V. Demchenko, and L. V. Wang, "Noninvasive photoacoustic computed tomography of mouse brain metabolism in vivo," *Neuroimage*, vol. 64, pp. 257–266, 2013.
- [10] M. Nasirivanaki, J. Xia, H. Wan, A. Q. Bauer, J. P. Culver, and L. V. Wang, "High-resolution photoacoustic tomography of resting-state functional connectivity in the mouse brain," *Proceedings of the National Academy of Sciences*, vol. 111, no. 1, pp. 21–26, 2014.
- [11] Y. Zhou, J. Yao, and L. V. Wang, "Tutorial on photoacoustic tomography," *Journal of Biomedical Optics*, vol. 21, no. 6, pp. 061007–061007, 2016.
- [12] J. Yao and L. V. Wang, "Photoacoustic microscopy," *Laser & Photonics Reviews*, vol. 7, no. 5, pp. 758–778, 2013.
- [13] M. Xu and L. V. Wang, "Time-domain reconstruction for thermoacoustic tomography in a spherical geometry," *IEEE Transactions on Medical Imaging*, vol. 21, no. 7, pp. 814–822, 2002.
- [14] Y. Xu, M. Xu, and L. V. Wang, "Exact frequency-domain reconstruction for thermoacoustic tomography. ii. cylindrical geometry," *IEEE Transactions on Medical Imaging*, vol. 21, no. 7, pp. 829–833, 2002.
- [15] Y. Xu, D. Feng, and L. V. Wang, "Exact frequency-domain reconstruction for thermoacoustic tomography. i. planar geometry," *IEEE Transactions on Medical Imaging*, vol. 21, no. 7, pp. 823–828, 2002.
- [16] Q. Sheng, K. Wang, T. P. Matthews, J. Xia, L. Zhu, L. V. Wang, and M. A. Anastasio, "A constrained variable projection reconstruction method for photoacoustic computed tomography without accurate knowledge of transducer responses," *IEEE Transactions on Medical Imaging*, vol. 34, no. 12, pp. 2443–2458, 2015.
- [17] Y. Han, V. Ntziachristos, and A. Rosenthal, "Optoacoustic image reconstruction and system analysis for finite-aperture detectors under the wavelet-packet framework," *Journal of Biomedical Optics*, vol. 21, no. 1, pp. 016002–016002, 2016.
- [18] C. Zhang, Y. Wang, and J. Wang, "Efficient block-sparse model-based algorithm for photoacoustic image reconstruction," *Biomedical Signal Processing and Control*, vol. 26, pp. 11–22, 2016.
- [19] C.-W. Wei, T.-M. Nguyen, J. Xia, B. Arnal, E. Y. Wong, I. M. Pelivanov, and M. O'Donnell, "Real-time integrated photoacoustic and ultrasound (paus) imaging system to guide interventional procedures: ex vivo study," *IEEE Transactions on Ultrasonics, Ferroelectrics, and Frequency Control*, vol. 62, no. 2, pp. 319–328, 2015.
- [20] E. Mercep, G. Jeng, S. Morscher, P.-C. Li, and D. Razansky, "Hybrid optoacoustic tomography and pulse-echo ultrasonography using concave arrays," *IEEE Transactions on Ultrasonics, Ferroelectrics, and Frequency Control*, vol. 62, no. 9, pp. 1651–1661, 2015.
- [21] T. Harrison and R. J. Zemp, "The applicability of ultrasound dynamic receive beamformers to photoacoustic imaging," *IEEE Transactions on Ultrasonics, Ferroelectrics, and Frequency Control*, vol. 58, no. 10, pp. 2259–2263, 2011.
- [22] M. Karaman, P.-C. Li, and M. O'Donnell, "Synthetic aperture imaging for small scale systems," *IEEE Transactions on Ultrasonics, Ferroelectrics, and Frequency Control*, vol. 42, no. 3, pp. 429–442, 1995.
- [23] T. Szasz, A. Basarab, and D. Kouamé, "Beamforming through regularized inverse problems in ultrasound medical imaging," *IEEE Transactions on Ultrasonics, Ferroelectrics, and Frequency Control*, vol. 63, no. 12, pp. 2031–2044, 2016.
- [24] N. Q. Nguyen and R. W. Prager, "High-resolution ultrasound imaging with unified pixel-based beamforming," *IEEE Transactions on Medical Imaging*, vol. 35, no. 1, pp. 98–108, 2016.
- [25] M. Sadeghi and A. Mahloojifar, "Improving beamforming performance by phased synthetic aperture imaging in medical ultrasound," *Journal of Medical Ultrasonics*, pp. 1–12, 2016.
- [26] B. M. Asl and A. Mahloojifar, "Minimum variance beamforming combined with adaptive coherence weighting applied to medical ultrasound imaging," *IEEE Transactions on Ultrasonics, Ferroelectrics, and Frequency Control*, vol. 56, no. 9, pp. 1923–1931, 2009.
- [27] A. M. Deylami and B. M. Asl, "Low complex subspace minimum variance beamformer for medical ultrasound imaging," *Ultrasonics*, vol. 66, pp. 43–53, 2016.
- [28] M. Bae, S. B. Park, and S. J. Kwon, "Fast minimum variance beamforming based on legendre polynomials," *IEEE Transactions on Ultrasonics, Ferroelectrics, and Frequency Control*, vol. 63, no. 9, pp. 1422–1431, 2016.
- [29] N. Nguyen and R. Prager, "Minimum variance approaches to ultrasound pixel-based beamforming," *IEEE Transactions on Medical Imaging*, 2016.
- [30] S. A. I. Avani, A. Mahloojifar, and B. M. Asl, "Adaptive 3d mv beamforming in medical ultrasound imaging," in *Biomedical Engineering (ICBME), 2013 20th Iranian Conference on*. IEEE, 2013, pp. 81–86.
- [31] P. Kruizinga, F. Mastik, N. de Jong, A. F. van der Steen, and G. van Soest, "Plane-wave ultrasound beamforming using a nonuniform fast fourier transform," *IEEE transactions on ultrasonics, ferroelectrics, and frequency control*, vol. 59, no. 12, pp. 2684–2691, 2012.
- [32] R. S. Bandaru, A. R. Sornes, J. Hermans, E. Samsset, and J. DáÁzhooge, "Delay and standard deviation beamforming to enhance specular reflections in ultrasound imaging," *IEEE Transactions on Ultrasonics, Ferroelectrics, and Frequency Control*, vol. 63, no. 12, pp. 2057–2068, 2016.
- [33] G. Matrone, A. S. Savoia, G. Caliano, and G. Magenes, "The delay multiply and sum beamforming algorithm in ultrasound b-mode medical imaging," *IEEE Transactions on Medical Imaging*, vol. 34, no. 4, pp. 940–949, 2015.
- [34] H. B. Lim, N. T. T. Nhung, E.-P. Li, and N. D. Thang, "Confocal microwave imaging for breast cancer detection: Delay-multiply-and-sum image reconstruction algorithm," *IEEE Transactions on Biomedical Engineering*, vol. 55, no. 6, pp. 1697–1704, 2008.
- [35] G. Matrone, A. Ramalli, A. Savoia, P. Tortoli, and G. Magenes, "High frame-rate, high resolution ultrasound imaging with multi-line transmission and filtered-delay multiply and sum beamforming," *IEEE Transactions on Medical Imaging*, 2016.
- [36] J. Park, S. Jeon, J. Meng, L. Song, J. S. Lee, and C. Kim, "Delay-multiply-and-sum-based synthetic aperture focusing in photoacoustic microscopy," *Journal of Biomedical Optics*, vol. 21, no. 3, pp. 036010–036010, 2016.
- [37] B. E. Treeby and B. T. Cox, "k-wave: Matlab toolbox for the simulation and reconstruction of photoacoustic wave fields," *Journal of Biomedical Optics*, vol. 15, no. 2, pp. 021314–021314, 2010.
- [38] J. Synnevag, A. Austeng, and S. Holm, "Adaptive beamforming applied to medical ultrasound imaging," *IEEE Transactions on Ultrasonics Ferroelectrics and Frequency Control*, vol. 54, no. 8, p. 1606, 2007.